

# 1 **On the use of a mesoscale masonry pattern representation in discrete** 2 **macro-element approach**

3 Federica Vadalà<sup>1</sup>, Valeria Cusmano<sup>2</sup>, Marco Francesco Funari<sup>1,\*</sup>, Ivo Caliò<sup>2</sup> and Paulo B. Lourenço<sup>1</sup>

4 <sup>1</sup>Department of Civil Engineering, University of Minho, ISISE, 4800-058 Guimarães, Portugal

5 <sup>2</sup>Department of Civil Engineering and Architecture (DICAR), University of Catania, Italy.

6 \*Correspondence: [marcofrancesco.funari@civil.uminho.pt](mailto:marcofrancesco.funari@civil.uminho.pt)

## 7 **Abstract**

8 This paper presents numerical investigations using the mesoscale approach coupled with the discrete  
9 macro-element approach for masonry structures, i.e., each macro-element represents a single unit stone.

10 At first, parametric analyses are performed on a U-shape masonry prototype made with stone. Nonlinear  
11 static analyses are performed to investigate parameters that affect the results when a mesoscale masonry  
12 pattern representation is adopted. Results demonstrate how mesoscale representation is a powerful  
13 alternative to model unreinforced masonry structures within a discrete macro-element approach  
14 (particularly if compared with classic homogeneous FE methodologies). However, one of the main  
15 challenges in using the mesoscale approach for the structural assessment of masonry buildings, made  
16 with stones having different dimensions, is the unit by unit description. The complexity of the problem,  
17 and the amount of information needed, usually preclude the study of these structures deterministically.  
18 To this end, a digital tool to generate randomised masonry patterns using a few input parameters is  
19 proposed. A box structure is adopted as parent geometry, and ten masonry patterns with different  
20 degrees of randomness are investigated by performing nonlinear static and dynamic simulations. The  
21 outcomes focus on the influence of masonry patterns and demonstrate how irregularity of units can  
22 affect the structural response leading to a reduction in terms of strength and ductility if compared to  
23 regular distribution of masonry units.

24 **Keywords:** Unreinforced masonry structures; Mesoscale approach; non-periodic masonry pattern;  
25 DMEM.  
26

## 27 **1 Introduction**

28 Field reconnaissance after earthquake events demonstrated how out-of-plane (OOP) failure mechanisms  
29 affect historical unreinforced masonry (URM) structures, producing their collapse, loss of life, and, at  
30 the same time, an immaterial loss of memory and people identity [1]–[3]. As a consequence, in the last  
31 decades, several researchers proposed advanced analysis methods, often calibrated through extensive  
32 experimental campaigns [4]–[9], for the preventive assessment of heritage buildings. Their overall  
33 classification is mainly made between numerical and analytical approaches [10], [11].

34 Analytical approaches are often based on limit analysis theorems that have the great advantage of being  
35 independent of most material properties but inevitably rely on a very simplified material model [12]–  
36 [15]. Such approaches include force- and displacement-based procedures suitable for rapid seismic  
37 vulnerability assessment. Moreover, limit analysis-based tools typically neglect the structure's global  
38 behaviour, only focusing on assessing a set of local failure mechanisms [16]–[20].

39 Numerical approaches are typically implemented in the Finite Element Method (FEM) [21]–[27] or  
40 Discrete Element Method (DEM) [28]–[32] frameworks. Such approaches model the masonry material  
41 using different representation scales, i.e., equivalent continuum, macro-blocks, or discrete  
42 representations. FEM allows a more versatile application as masonry can be represented either through  
43 a homogeneous equivalent media (designated macro-modelling) or by a discrete representation of units  
44 and joints (designated micro-modelling). DEM is well suited for masonries with both dry- and mortared  
45 joints but still requires a full representation of the blocks (masonry units) arrangement [32]–[37]. In  
46 both cases, linear and nonlinear static and dynamic analyses are eligible.

47 Nonetheless, additionally, to the significant amount of data needed to characterise the nonlinear  
48 response of materials, the analysis can be both time-consuming and computationally expensive when  
49 estimating the ultimate ductility level of the structure. Despite their reliability, the computational  
50 efficiency of the available numerical methods is rarely compatible with the need to have a rigorous real-  
51 time post-earthquake assessment [38]. Hence, several research groups developed alternative modelling  
52 approaches and practical tools to decrease the computational cost of nonlinear static and dynamic  
53 analyses [39]–[42].

54 In this framework, macro-element approaches were proposed in which structures are described as an  
55 assemblage of macroscopic structural elements. For instance, the Equivalent Frame Model (EFM) is  
56 being adopted by national and international standards in combination with nonlinear static analysis [43].  
57 Because of its simplicity and low computational demand, it is one of the most widely adopted analysis  
58 methods in engineering practice [44]. However, despite the advantages of the EFM method, it is worth  
59 underlining some limitations: i) discretisation of structure with an irregular position of openings is  
60 sometimes ambiguous or not possible, ii) geometric inconsistency of the approach, as it represents a  
61 plane portion such as masonry panels with a mono-dimensional element, iii) presence of areas which  
62 cannot be damaged, generally identified as rigid links, iv) the ultimate displacement is a priori defined.

63 In order to cover such limitations and keep the computational efficiency, a discrete macro-element  
64 method (DMEM) was proposed in Ref. [45]. The first implementation of the DMEM approach was  
65 based on a plane element whose kinematics was described only by four Lagrangian parameters: three  
66 degrees of freedom associated with the in-plane (IP) rigid-body motion and one additional degree of  
67 freedom related to shear deformability in its own plane. Such plane elements were represented by  
68 articulated quadrilaterals with rigid edges connected to the vertices by four hinges and diagonal springs  
69 simulating the shear behaviour. Each element was connected to the adjacent ones by means of a discrete  
70 distribution of nonlinear springs, denoted as interfaces. The interfaces' deformations are associated with  
71 the relative motion of the connected panels, and no additional Lagrangian parameters are needed. One  
72 can note how this preliminary formulation of the DMEM approach simulated the nonlinear behaviour  
73 of masonry panels IP, not being able to describe the out-of-plane (OOP) behaviour. The reliability of  
74 the proposed approach was evaluated by means of nonlinear incremental static analysis performed on  
75 masonry structures, for which theoretical and/or experimental results are available in the literature [45].  
76 Afterwards, the macro-element was improved to investigate OOP response of URM structure by  
77 developing a three-dimensional macro-element for which its kinematic was described by seven degrees  
78 of freedom IP and OOP [46]. Subsequently, such an element was adopted to simulate also curved  
79 masonry structures, whose role is fundamental both in the local and global behaviour of the buildings,  
80 especially in the monumental ones (e.g. arches, vaults, and domes) [47]. Both experimental and  
81 numerical validations showed the capability of the proposed approach to be applied to predict the

82 nonlinear response of URM structures under different loading conditions. A more recent  
83 implementation was conducted to assess the seismic behaviour of URM structures subjected to dynamic  
84 input, i.e., earthquakes records, by introducing a consistent or lumped mass matrix [48]. As  
85 demonstrated in Ref. [48], the DMEM strategy showed its capability to simulate dynamic response  
86 characterised by coupling IP/OOP failure mechanisms. Despite the improvements recently  
87 implemented in the DMEM approach, some limitations still characterised such a methodology, i.e., i)  
88 formulation accounts only for small displacements, ii) macro elements size dependency when the  
89 structure is affected by OOP loading, iii) vertical joints do not permit to account for interlocking  
90 phenomenon typically expected in masonry structures. However, the literature analysis underlines how  
91 the DMEM approach may be used to assess the seismic behaviour of historic masonry structures.  
92 Nevertheless, just a few attempts investigated the influence of the mesh discretisation of the macro-  
93 elements, how the same impacts the structural response, and the potential in adopting a mesoscale  
94 representation [49]. In order to address these gaps, this paper mainly aims to: i) apply the DMEM  
95 approach by adopting a mesh representation consistent with real masonry patterns and ii) evaluate what  
96 phenomenon affects the structural response. To accomplish the latter, the framework described next has  
97 been followed:

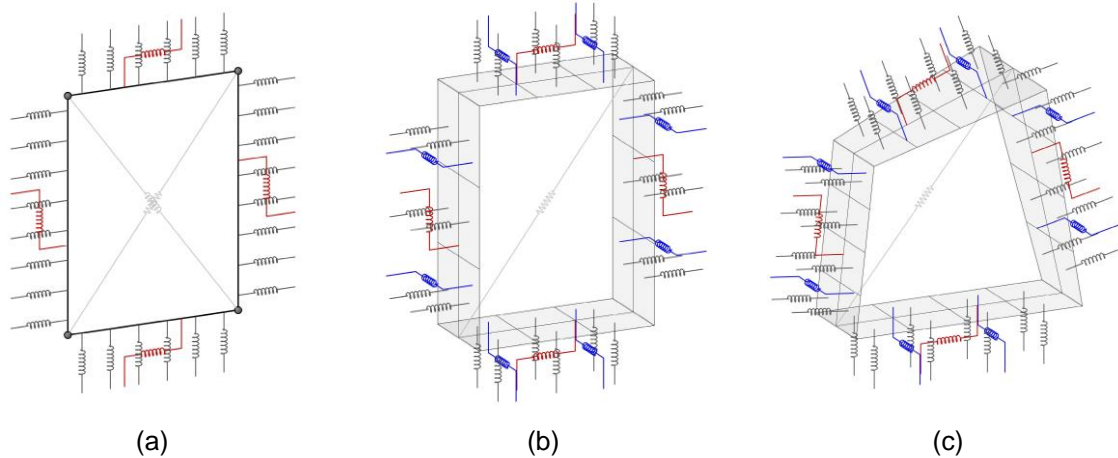
- 98 1. The 3D macro-element is adopted to simulate the OOP response of masonry structures.
- 99 2. Parametric investigations are performed on U-shape masonry prototypes made with stone [50].  
100 Modelling parameters are investigated and discussed, and the motivation in using mesoscale  
101 mesh discretisation is underlined.
- 102 3. A random mesh generator is implemented to quickly generate numerical models where the  
103 masonry patterns are consistent with a chaotic distribution of the units.
- 104 4. The random mesh generator tool is used to generate ten different masonry patterns consistent  
105 with a unique parent geometry. The masonry prototypes differ only in terms of masonry patterns  
106 and openings.

107 The novelties of the study include: i) a pioneering application of the mesoscale random generated  
108 masonry pattern representation in DMEM for simulating unreinforced masonry structures, ii) numerical

109 investigation of the phenomenon that affects the structural response when mesoscale representation is  
110 adopted, and iii) implementation of a visual script for the generation of different masonry wall patterns.  
111 The paper is organised as follows. Section 2 summarises the theoretical formulation and the numerical  
112 implementation of the DMEM approach. Section 3 presents a parametric study to assess how the mesh  
113 topology affects the structural response and reports comparisons between classical DMEM and finite  
114 element homogenous approaches. Section 4 investigates how different degrees of randomness affects  
115 the seismic behaviour of a benchmark case. Finally, conclusions are discussed in Section 5.

## 116 **2 Discrete Macro-Element Modelling Approach**

117 As mentioned in the previous section, the original formulation of the DMEM approach provided only  
118 the possibility to simulate the IP structural response of masonry panels, which were modelled using a  
119 simple plane element (Figure 1a). In order to overcome this issue, a macro-element that was able to  
120 simulate the OOP response was proposed in Ref. [47]. Such a macro-element is a zero-thickness  
121 element, which is able to account for shear deformation in its plane, having on the edges a set of different  
122 nonlinear links denoted as interfaces. Each interface is constituted by i)  $m$  rows of  $n$  orthogonal  
123 nonlinear links, responsible for simulating the panels' flexural behaviour (Figure 1b and Figure 1c), ii)  
124 a single IP sliding link, which rules for the sliding behaviour, and iii) a set of two OOP sliding links  
125 that account for both OOP sliding and torsional behaviour. One can note that the number of orthogonal  
126 links is selected in accordance with the desired level of accuracy, losing as a counterpart a little  
127 computational efficiency. The diagonal shear deformability is governed by a diagonal nonlinear link  
128 that connects two corners of the quad element [46]. Hence, the kinematics of the spatial macro-element  
129 are described by seven Lagrangian parameters, six governing the rigid body motion and the remaining  
130 associated with the IP shear deformability. One can note that the low number of DOFs associated with  
131 each macro-element makes this approach computationally inexpensive with respect to the classical  
132 FEM and DEM formulations.



133 Figure 1: DMEM evolution (a) Plane Element; (b) Regular Spatial Element; (c) Irregular Spatial Element.

134 Macro-element's nonlinear links calibration has been performed according to a straightforward fibre  
 135 calibration procedure. The procedure reported herein is suitable for three-dimensional model  
 136 characterised by elements with the same geometrical and mechanical characteristics. Nevertheless, the  
 137 calibration procedure of nonlinear links associated with irregular three-dimensional panels  
 138 characterized by different mechanical properties presents a more sophisticated procedure beyond this  
 139 research's scope. A detailed description of the calibration procedure for irregular macro-elements, can  
 140 be found in Ref. [51]. The nonlinear interface's links can be distinguished as transversal N-links, IP  
 141 shear sliding N-link, and OOP shear sliding N-links. In the following, the main characteristics of the  
 142 calibration procedure are described with reference to each group of nonlinear N-links.

143 Transversal N-links orthogonal to the interfaces govern the flexural IP and OOP behaviour between  
 144 two adjacent macro-elements. Each orthogonal link is representative of the nonlinear behaviour of the  
 145 corresponding masonry strip of two adjacent elements (e.g. panels  $l$  and  $k$ ) along a given material  
 146 direction. Since the deformations of the panels are concentrated in the zero-thickness interfaces, the  
 147 orthogonal links have the role of simulating the deformability of the two connected panels in a given  
 148 direction. It is worth noting that to account for masonry as an orthotropic material, the calibration is  
 149 conducted separately for horizontal and vertical interface elements. The initial stiffness  $K_n$  of each link  
 150 is simply obtained by assigning, to each link, the axial rigidity (Young's modulus,  $E$ ) of the  
 151 corresponding masonry strip defined by the volume characterised by the influence area ( $A_{Sn}$ ) of each  
 152 spring and half of the length ( $L/2$ ) of the panel (Figure 2a). This procedure provides a couple of springs

153 in series, each associated with each of the connected panels. Each couple of springs is then replaced by  
154 a single resulting nonlinear spring as described in [45]. The yielding forces in tension,  $F_{ym}$ , and  
155 compression,  $F_{ycn}$ , of each transversal link are related to their influence area and the tensile,  $\sigma_t$ , and  
156 compressive strengths,  $\sigma_c$ , adopted for the masonry. Finally, the tensile and compressive yieldind  
157 displacements  $u_{ym}$  and  $u_{ycn}$  are associated with each link's yielding forces and initial stiffness. The  
158 nonlinear behaviour of the masonry can be simulated by adopting for transversal links any suitable and  
159 uniaxial nonlinear constitutive laws. Initial stiffness, tensile and compressive strength and displacement  
160 are reported respectively in Eq. 1-5.

$$161 \quad K_n = 2 \frac{EA_{Sn}}{L} \quad (1)$$

$$162 \quad F_{ytn} = A_{Sn} \sigma_t \quad (2)$$

$$163 \quad F_{ycn} = A_{Sn} \sigma_c \quad (3)$$

$$164 \quad u_{ytn} = \frac{F_{ytn}}{K_n} \quad (4)$$

$$165 \quad u_{ycn} = \frac{F_{ycn}}{K_n} \quad (5)$$

166 The shear deformation of a masonry wall, discretised by a mesh of macro-elements, can be partly related  
167 to the diagonal shear deformation and partly due to the friction sliding along the interface between two  
168 adjacent macro-elements. The former is governed by a single diagonal spring (Figure 1) connecting two  
169 opposite macro-elements vertexes. First, a linear elastic calibration is performed by enforcing the  
170 equivalence between the macro-element subjected to a pure shear deformation related to the kinematic  
171 of the hinged quadrilateral and a reference continuous elastic solid. This finite portion of masonry is  
172 characterised by shear modulus  $G$ , transversal area  $A_r$ , height  $h$ , and base  $b$ . The initial stiffness  $K_D$  of  
173 the diagonal link is expressed in Equation 6, in which  $\theta$  is defined as  $\arctan(b/h)$ , and it is influenced by  
174 a shear factor denoted as  $\alpha_s$ , whose value ranges between 0 and 1. If this factor presents a value equal to  
175 1, the global in-plane shear stiffness is entirely associated with the initial stiffness of the diagonal links,  
176 and the in-plane sliding links are assumed rigid. On the other hand, if the value of  $\alpha$  is different from 1,  
177 the global in-plane shear stiffness comes as a contribution between diagonal and in-plane sliding  
178 nonlinear links.

179 
$$K_D = \frac{G \cdot A_t}{h \cdot \cos^2 \theta \cdot \alpha_s} \quad (6)$$

180 The nonlinear post-elastic behaviour may be addressed by adopting different and suitable constitutive  
 181 laws. A Mohr-Coulomb or Turnsek-Cacovic yielding criteria can be adopted for the constitutive  
 182 calibration of this nonlinear link. The value of yielding force  $F_y$  associated to the Mohr-Coulomb and  
 183 Turnsek and Cacovic [52] criteria are given by Equations 7 and 8, respectively.

184 
$$F_y = F_{y0} + \mu_d \cdot N \quad (7)$$

185 
$$F_y = F_{v0} \sqrt{1 + \frac{N}{1.5 \cdot F_{v0}}} \quad (8)$$

186 where  $F_{y0}$  and  $F_{v0}$  are the yielding forces under no confinement conditions (zero normal stresses)  
 187 associated with the Mohr-Coulomb or Turnsek-Cacovic criteria.

188 The IP and OOP shear sliding springs (Figure 2b) rule the relative sliding motion between two adjacent  
 189 macro-elements. The initial stiffness  $K_S$ , related to the sliding mechanism, is associated with the panel's  
 190 shear modulus  $G$ , the effective length, and the influence area  $A_s$  of the corresponding nonlinear link.  
 191 The expression that provides the initial stiffness for IP and OOP sliding links is given by Equation 9. It  
 192 is worth mentioning that the OOP shear mechanism is solely associated with the nonlinear links along  
 193 the thickness of the interface element, and there is no need to introduce a shear factor in the out-of-  
 194 plane direction. The OOP sliding links also account for torsional behaviour around the axis orthogonal  
 195 to the interface plane (Figure 2c). The elastic torsional stiffness  $K_\phi$  is associated with a torsional rigidity  
 196 factor  $J_\phi$  given by Equation 11, in which  $s$  corresponds to the thickness of the panel. The shear sliding  
 197 behaviour of UMR structure is associated with a frictional phenomenon along the mortar joints. Such  
 198 behaviour can be adequately simulated by means of a Mohr-Coulomb yielding criterion. Based on this  
 199 approach, the current yielding force  $F_y$  of the IP and OOP links is defined employing the cohesion  $c$   
 200 and friction coefficient  $\mu_s$ , of the masonry material, the current contact area  $A$ , and the normal force  $N$   
 201 applied to the interface element.

202 
$$K_S = \frac{G \cdot A_s}{L \cdot (1 - \alpha_s)} \quad (9)$$

203

204

205

206

$$K_\phi = \frac{G \cdot J_\phi}{L} \quad (10)$$

207

$$J_\phi = B \cdot s^3 \left[ \frac{1}{3} - 0.21 \frac{s}{B} \left( 1 - \frac{s^4}{12 \cdot B^4} \right) \right] \quad (11)$$

208

$$F_y = c \cdot A + \mu_s \cdot N \quad (12)$$

209

210

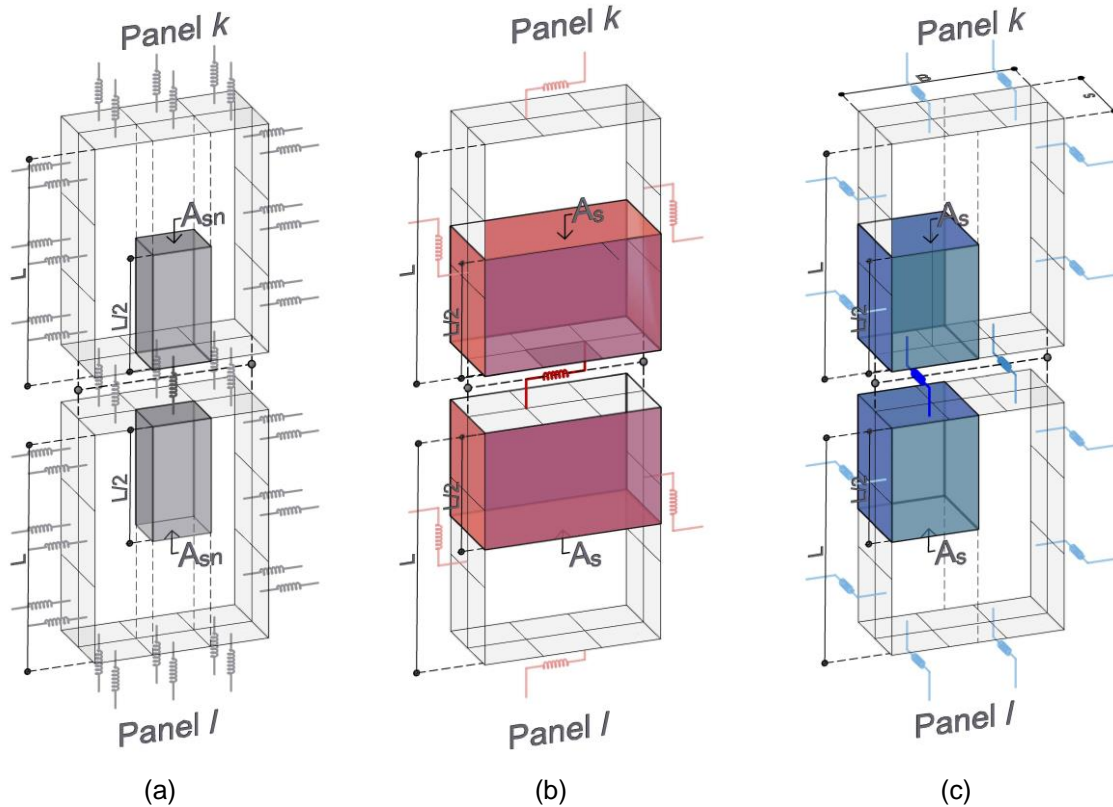
211

212

213

214

More details on the calibration procedures can be found in Refs. [45], [46]. One can note that different nonlinear constitutive laws for the shear mechanisms accounting for residual strength when a target displacement is attained might be adopted. However, it has not been considered in the present paper since the main goal of this study relies on the investigation of the masonry mesoscale masonry pattern representation in a DMEM approach. For this reason, simple constitutive laws have been adopted aiming at limiting the number of parameters involved in the numerical analyses.



215

216

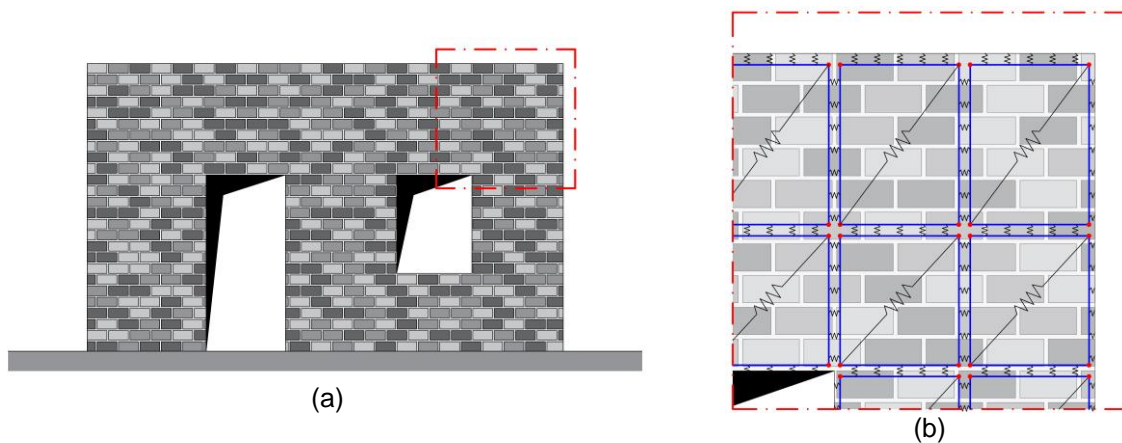
Figure 2: Interface's Links representation: (a) Orthogonal N-Links; (b) In-plane sliding N-links; (c) Out-of-Plane sliding N-Links.

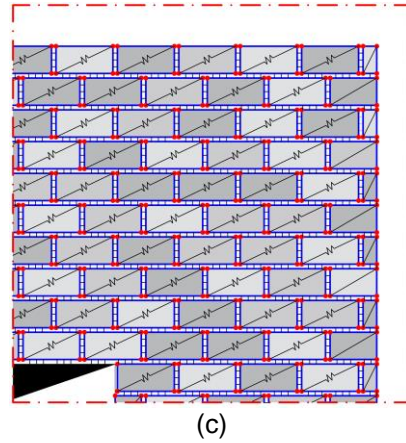
217

218

DMEM approach classical interpretation implies that each macro-element must be representative of the corresponding finite portion of masonry walls, according to the macro-modelling approach.

219 Consequently, there is no relation between masonry constituents and block regions, and a  
220 homogenisation strategy is adopted to define the masonry mechanical constitutive law.  
221 An example of a masonry wall is shown in Figure 3a. Even though DMEM is conceived as a macro-  
222 modelling strategy, some studies (Figure 3b) explored the possibility of discretising the structural model  
223 within a mesoscale approach (Figure 3c) [49], [53]. In this case, the properties of the constituents, for  
224 example, brick and mortar, and the details of the masonry arrangement are adopted to study the  
225 interaction of the constituents and the damage propagation pattern under different loading histories. It  
226 is worth noting that by using mesoscale strategies, some physical phenomena involved can be described  
227 in more detail, i.e. interlocking effect between the blocks or the presence of well-defined and realistic  
228 fracture surfaces at the interface. Moreover, a mesoscale model is quite accurate for the study of weak  
229 or dry mortar masonry structures for which usually DEM approaches are adopted [28], [29], [54].  
230 Therefore, depending on whether a macro- or mesoscale approach is adopted, it is necessary to  
231 appropriately calibrate the main mechanical parameters that influence the response. As reported in Ref.  
232 [49], the interlocking phenomenon has mainly the effects of increasing the tensile strength and the  
233 cohesion between blocks influencing the collapse mechanism and increasing the strength and  
234 displacement capacity of the entire structure.





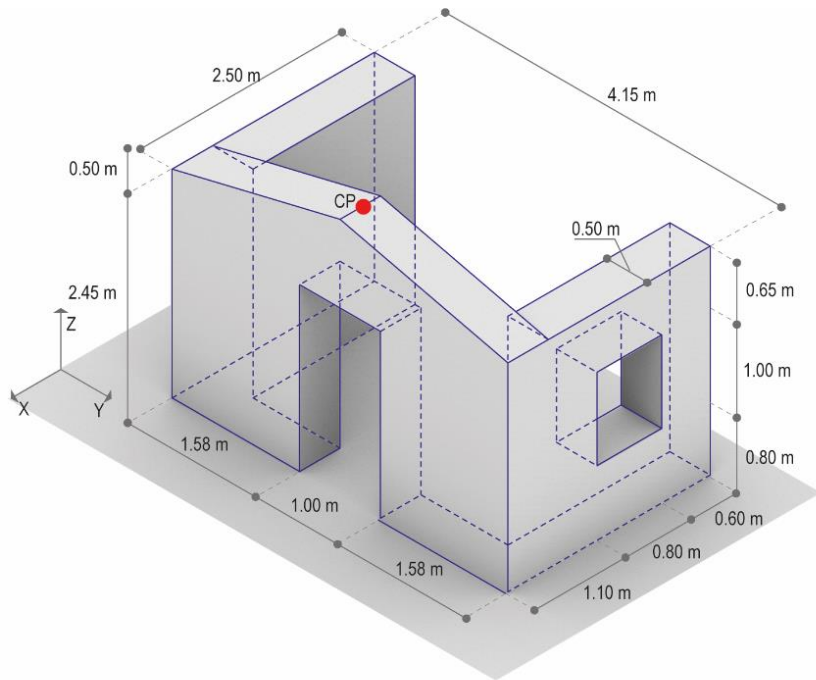
235 Figure 3: (a) Real blocks' arrangement; (b) Macro-scale modelling; (c) Mesoscale modelling.

236

### 237 3 Numerical Investigation: U-shape Stone Prototype

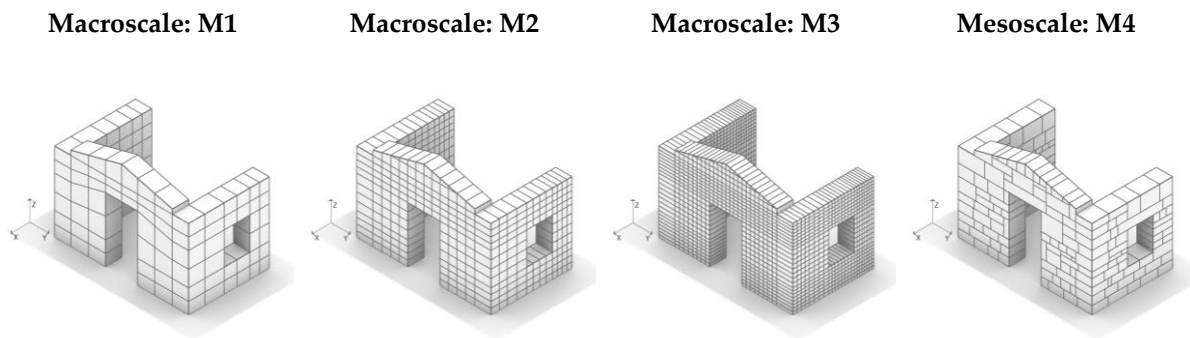
#### 238 3.1 Description of the prototype

239 In this section, parametric studies are performed to assess how the mesh topology affects numerical  
 240 simulations performed with the DMEM. The numerical investigation has been performed on a  
 241 benchmark represented by a U-shape masonry prototype, a simple structure of three walls forming a U-  
 242 plan made in stone masonry that idealises the experimental tests performed at the LNEC shaking table  
 243 [55]. Figure 4 represents the overall geometrical characteristic of the masonry prototype.



244 Figure 4: U-Shape stone prototype: geometrical features.  
 245

246 Figure 5 represents the different mesh discretisations adopted. Three of them are mesh discretisations  
 247 consistent with the macroscale approach, in which the macro-elements' characteristic dimension is  
 248 gradually decreased to reach three different levels of refinement. The last one is a mesoscale  
 249 discretisation, which is taken in agreement with the one adopted in Ref. [56]. Concerning the  
 250 mechanical properties, the parameters reported in Ref. [56] have been initially adopted for all mesh  
 251 discretisations (Table 1 and  
 252 Table 2). It is worth underlining that when a mesoscale representation is adopted (M4), a linear-elastic  
 253 constitutive law has been selected for the diagonal shear behaviour to avoid that diagonal cracking  
 254 involves the single macro element. This assumption ensures that the shear failure does not occur when  
 255 macro-element represents a single masonry unit [49].



256 Figure 5: Mesh discretisations adopted for the numerical investigations.

257  
 258 Table 1: Mechanical properties adopted for the U-shape prototype: flexural behaviour [56].

Model	Flexural behaviour					
	Density [kg/m <sup>3</sup> ]	Young's modulus [MPa]	Compressive strength [MPa]	Compressive fracture energy [N/mm]	Tensile strength [MPa]	Tensile fracture energy [N/mm]
M1,M2,M3	2360	2077	5.44	∞	0.224	0.048
M4	2360	2077	5.44	∞	0.224	0.048

259

260 Table 2: Mechanical properties adopted for the U-shape prototype: shear behaviour [56].

Model	Diagonal cracking behaviour			Sliding behaviour		
	Shear modulus [MPa]	Failure criterion	$\tau_0$ [MPa]	$\mu_d$	$c$ [MPa]	$\mu_s$
M1,M2,M3	830	Mohr-Coulomb	0.336	0.3	0.336	0.3
M4	830	-	-	-	0.336	0.3

261

## 262 **3.2 Nonlinear static analyses**

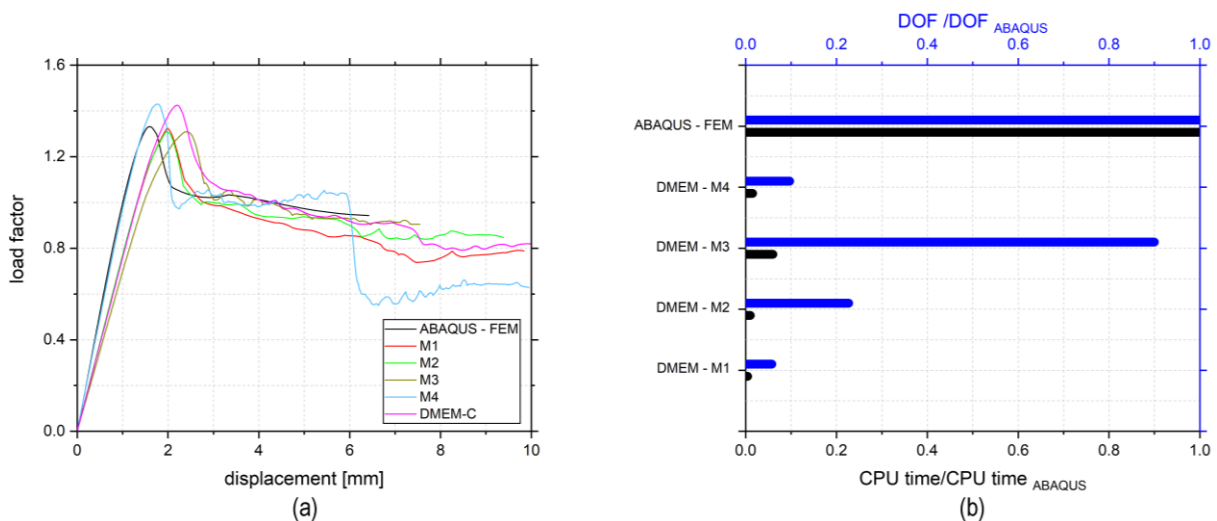
263 This section aims to investigate how the structural response of macro- and mesoscale masonry  
264 representations are adopted. Nonlinear static analyses have been performed applying vertical actions  
265 including gravity loads and, subsequently, an incremental lateral force along the positive direction of  
266 axis X.

267 Figure 6a reports the load-displacement curves of the considered mesh discretisations for horizontal  
268 actions. Further comparison is provided with a homogeneous model performed in Abaqus [57] where  
269 concrete damage plasticity (CDP) has been adopted to simulate the nonlinear behaviour of the masonry.

270 The results demonstrate how the M1, M2 and M3 models are slightly affected by a mesh dependency,  
271 showing small differences in terms of initial stiffness and peak load. On the contrary, the mesoscale  
272 model, i.e., M4, provides a stiffer initial behaviour and a higher peak load than the M1, M2 and M3.  
273 One can note how M4 has the same initial stiffness as the homogeneous model performed in Abaqus;  
274 however, the reached peak load is slightly higher than the macroscale discretisations, which cannot  
275 account for blocks' interlocking. When mesh discretisation with interlocking between blocks are  
276 considered, the structural response is characterised by a complex interaction between the macro-  
277 elements that involved shear sliding, shear diagonal, torsional, and membrane behaviour.

278 The mesoscale model M4 correctly accounts for the stone's interlocking effects leading to higher  
279 stiffness and ultimate load. Moreover, M1, M2 and M3 present similar post-peak behaviour, while M4  
280 has two drops. Generally, when a discrete numerical model is used, each drop corresponds to a local  
281 crack in the numerical model. Once again, the differences in the post-peak behaviour can be justified  
282 by the fact that the mesoscale model M4 correctly accounts for the stone's interlocking effects, leading  
283 to different and more realistic results in terms of loading-displacement curve and collapse mechanism.  
284 In this latter model, the first drop, in the loading-displacement curve, is due to the crack propagation  
285 that starts from the opening in the later wall, whereas the second drop is related to the flexural rocking  
286 mechanism of the orthogonal wall without openings in its plane, which causes compressive and tensile  
287 stresses at the base of the wall. When the tensile stress exceeds the tensile strength assumed for the

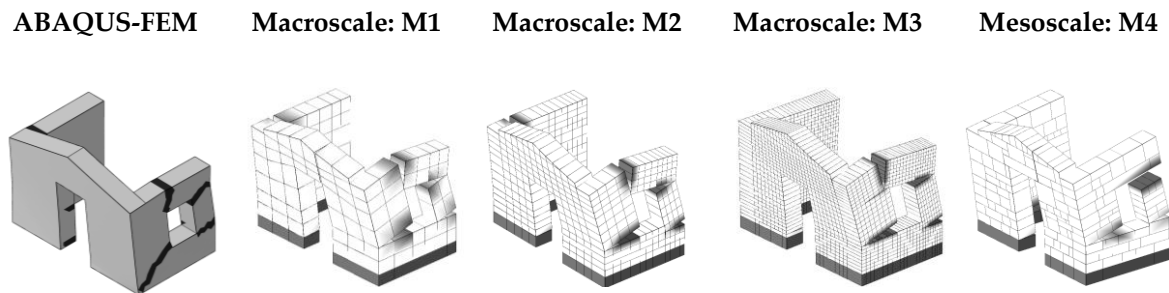
288 masonry, cracks propagate at the base of the wall. M4 model grasps the so-called flange effect that can  
 289 cause a significant overstrength on the approach based on equivalent frame modelling [58].  
 290 The misalignment of the vertical interfaces of the model M4 leads to more realistic results also in terms  
 291 of collapse mechanisms, as reported in Figure 7, where the failure mechanisms provided by the five  
 292 considered models are compared. To this end, for taking into account the interlocking effects provided  
 293 by the mesoscales model by using a macroscale simulation, it is needed to consider the over-stiffness  
 294 and over-strength in the calibration of the mechanical parameters, particularly when the size of the units  
 295 is large in comparison of the size of the structural components of the building. According to Ref. [31],  
 296 the tensile strength and fracture energy have been modified to obtain pushover curves comparable to  
 297 those relative to the mesoscale model. Hence, the updated macroscale model (DMEM-C) has the same  
 298 mesh discretisation adopted for M1, whereas tensile strength and fracture energy were calibrated  
 299 through a tuned process, which was stopped when assumed a value equal to 0.240 MPa and 0.060  
 300 N/mm, respectively.



301  
 302 Figure 6: (a) Comparison in terms of load-displacement curve; (b) Normalised computational time (CPU) and  
 303 normalised number of degrees-of-freedom (DOFs) for each numerical simulation.

304 One can note how M4 and DMEM-C curves show a different initial stiffness. Such a phenomenon may  
 305 be mitigated by also modifying the elastic modulus of the masonry in the DMEM-C model. Finally,  
 306 Figure 6b reports a comparison including the required computational time (CPU) and the number of  
 307 degrees-of-freedom (DOFs) for each mesh discretisation. Results have been normalised with respect to  
 308 the Abaqus model. It should be noted how the DMEM approach can strongly decrease the

309 computational demand, by more than 90%. Besides, when a mesoscale mesh representation has been  
310 used, the computational saving is more than 95%, while the amount of DOFs is decreased by 90%.



311 Figure 7: Comparison in terms of failure mechanisms.

312 In short, the mesoscale representation may be a powerful alternative to model unreinforced masonry  
313 structures within a discrete macro-element approach (particularly if compared with classic  
314 homogeneous FE methodologies), even though the mechanical calibration cannot be performed  
315 considering an equivalent homogenous masonry, as described in the previous section 2. Differently, a  
316 proper characterisation of the blocks and the mortar joints must be considered.

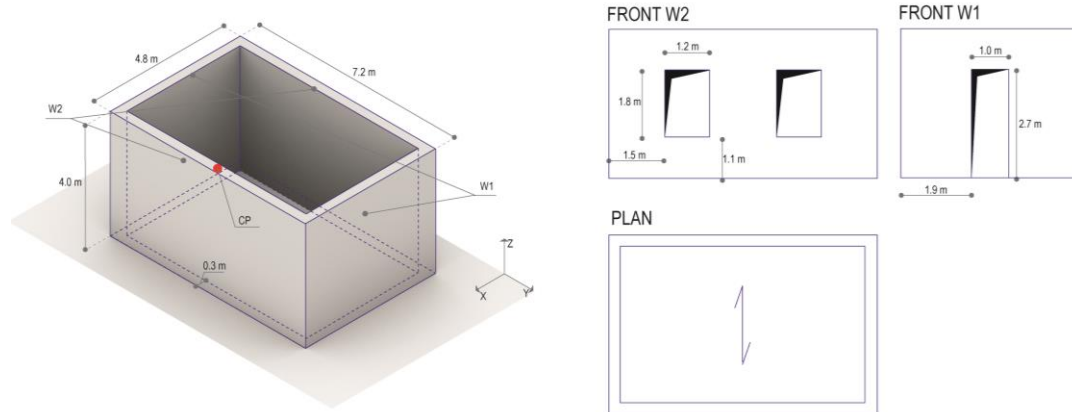
## 317 **4 Numerical Investigation: Box prototype**

### 318 **4.1 Generation of the models: geometrical and mechanical characteristics**

319 As reported in Ref. [59], masonry constituted by the assemblage of blocks and stones with variable  
320 dimensions is very common in historical buildings. However, the complexity of the problem, and the  
321 amount of information to accurately model using a mesoscale approach, usually preclude the study of  
322 these structures deterministically. Indeed, such uncertainties suggest investigations based on  
323 probabilistic approaches rather than deterministic, i.e., assuming texture properties within certain  
324 statistical variations.

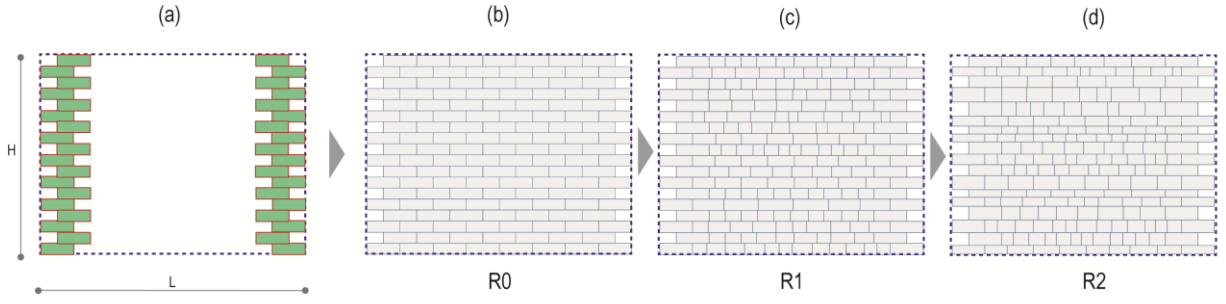
325 This section is devoted to understanding how irregular masonry patterns affect the structural response  
326 of a masonry prototype having a rectangular shape. Several mesh discretisations having a different  
327 degree of randomness have been generated by adopting a proper numerical tool which is described  
328 below. Instead, the parent geometry is always the same and coherent with a rectangular plan having  
329 4.80 m and 7.20 m, with walls' height equal to 4.0 m and a walls' thickness of 0.30 m (Figure 8). The

330 overload arising from a deformable slab, having a weight equal to 150 kN/m<sup>2</sup>, has been modelled as  
331 distributed line load along the top of the walls W2 (Figure 8).



332  
333 Figure 8: Parent geometry for box prototype: geometrical features.

334 The masonry patterns have been generated using a numerical tool implemented in a GHPython script  
335 [42], [43]. It can generate 2D or 3D masonry prototypes within a randomised masonry pattern. However,  
336 one can note that the GHPython script is responsible for generating a single planar wall, whereas the  
337 assemblages in 3D still require operations performed that have been manually implemented. Next, the  
338 tool's explanation is performed in 2D framework, i.e., referred to the generation of a single planar wall.  
339 As represented in Figure 9a, the primary tool's inputs are the overall dimension of the wall (height,  
340 length and width), the cantonal's dimension, and the number of units' courses ( $N_R$ ). At this stage, the  
341 user has to define some parameters defining three numerical domains. As reported in Figure 9b the first  
342 domain is formed by integer numbers that define the minimum and the maximum number of units per  
343 row ( $U_R$ ). The second domain of values is defined by the smallest and the largest unit length that may  
344 appear at each row ( $U_L$ ). Finally, the third domain, similar to the second one, is defined by the minimum  
345 and maximum height that may assume a units' course ( $U_H$ ) (Figure 9c). Finally, the total height of the  
346 wall is scaled in order to be consistent with the primary input of the generator. The proposed algorithm  
347 can randomise the values contained inside the early mentioned domains and generate a different  
348 masonry pattern at each iteration.



349

350 Figure 9: Random masonry pattern generation.

351 Referring to the parent geometry reported in Figure 8, one can note that two subcategories of masonry  
 352 patterns have been generated, which are characterised by a different number on the units' courses equal  
 353 to (A) 18 and (B) 12, respectively. The investigated mesh configurations are reported in Figure 10. A  
 354 regular masonry bond pattern characterises the reference configurations A1 and B1, where all the units  
 355 have the same dimensions, i.e.,  $0.60 \times 0.222 \times 0.30 \text{ m}^3$  and  $0.60 \times 0.333 \times 0.30 \text{ m}^3$ , respectively.

356 A chaotic mesh distribution instead characterises A2 and B2 configurations. Therefore, the following  
 357 values for the domains  $U_R$  and  $U_L$  have been adopted:

358 
$$U_R^{W1} = [6, 10] \quad (13)$$

359 
$$U_R^{W2} = [9, 15] \quad (14)$$

360 
$$U_L^{W1,W2} = [[0.20, 0.60], 1.00] \quad (15)$$

361 where the limits W1 and W2 are referred to walls having smaller and larger lengths (see Figure 9). One  
 362 can note how  $U_L^{W1,W2}$  does not contain the actual dimension of the blocks, but the ratio between a lower  
 363 bound, which has been assumed to be randomly selected between 0.20 and 0.60, and the upper bound  
 364 that is equal to 1.00. The value selection is random and is performed by using the random function  
 365 available in Python [60]. Hence, a remapping procedure must be performed in order to respect the  
 366 compatibility condition regarding geometry:

367 
$$\sum_{U_R} U_L / (L - L_{cant}) = 1 \quad (16)$$

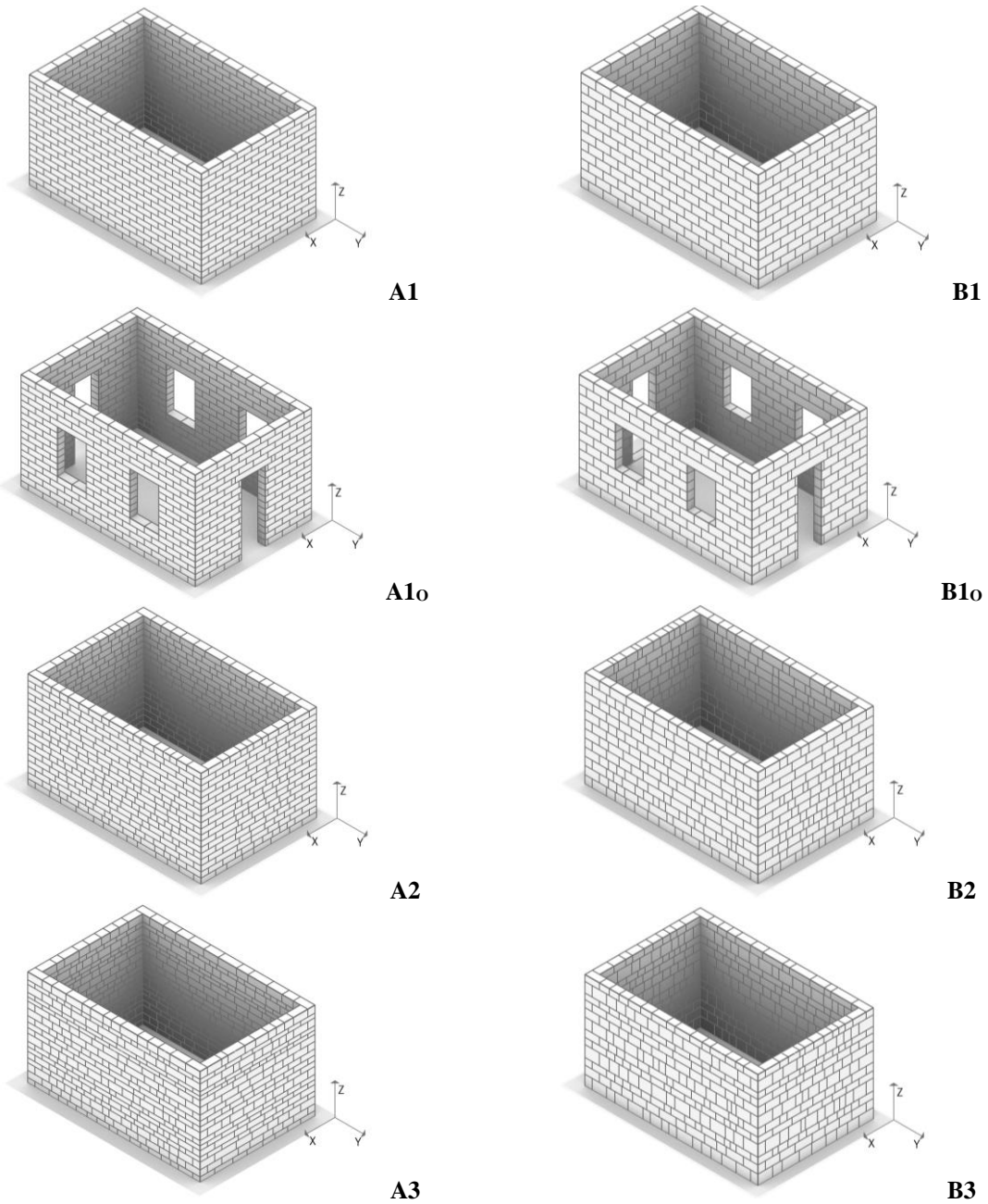
368 Finally, A3 and B3 are also affected by a variable height of the units' courses. In this case, the domain  
 369  $U_H$  has been defined as follow:

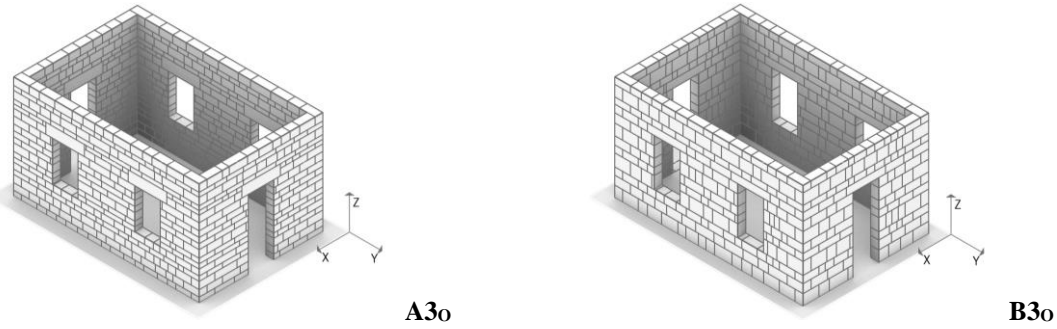
370 
$$U_H = [0.50, 1.00] \quad (17)$$

371 One can note that  $U_H$  does not contain the actual height of the unit's course, but the ratio between a  
 372 lower bound, assumed to be 0.50, and the upper bound that is equal to 1.00. Hence, a remapping  
 373 procedure must be again performed in order to respect the following compatibility condition:

374 
$$\sum_{N_R} U_H/(H) = 1 \tag{18}$$

375 Finally, the openings are added by making Boolean differences and introducing the lintels.





376  
377 Figure 10: Mesh discretisations adopted for the numerical investigations, with a total of ten.

378 As mentioned in section 2, DMEM approach requires defining the mechanical properties considering  
379 the failure modes, i.e., flexural, shear-diagonal and shear-sliding, independently. A  
380 nonlinear constitutive law has been assumed for the flexural response, governed by an exponential  
381 softening for the tensile post-peak behaviour and a parabolic curve for the compressive post-peak  
382 behaviour. The shear-sliding behaviour has been considered according to a Mohr-Coulomb failure  
383 criterion, considering a perfectly post-elastic constitutive law and assuming that the cohesion under no  
384 confinement conditions is equal to the tensile strength. Regarding the shear-diagonal behaviour, a  
385 linear-elastic constitutive law has been adopted to avoid the shear failure of the element, i.e., a  
386 mesoscale approach [56] without accounting for the failure of the units (assumed infinitely resistant).  
387 Table 3 and Table 4 summarise the mechanical properties adopted across the numerical simulation. One  
388 can note how tensile strength and fracture energy have been assumed to be very small to simulate dry-  
389 stacked masonry.

390 Table 3: Mechanical properties adopted for the box prototype: flexural behaviour

	Flexural behaviour					
	Density	Young's modulus	Compressive strength	Compressive fracture energy	Tensile strength	Tensile fracture energy
Model	[kg/m <sup>3</sup> ]	[MPa]	[MPa]	[N/mm]	[MPa]	[N/mm]
Mesoscale	1800	1500	3.80	3.00	0.001	0.0001

391  
392  
393 Table 4: Mechanical properties adopted for the box prototype: shear behaviour

	Diagonal cracking behaviour			Sliding behaviour		
	Shear modulus	Failure criterion	$\tau_0$	$\mu_d$	$c$	$\mu_s$
Model	[MPa]		[MPa]		[MPa]	
Mesoscale	580	-	-	-	0.001	0.6

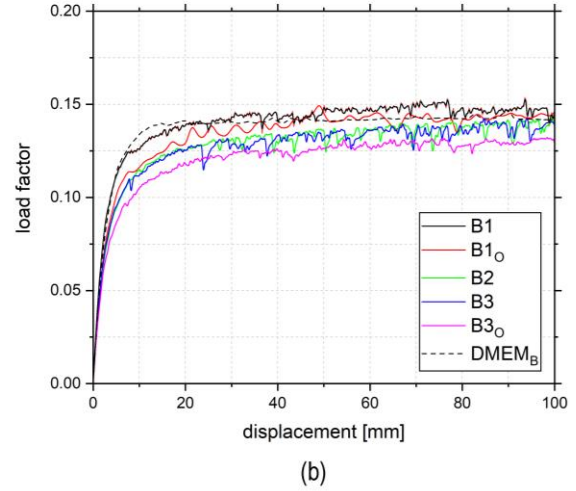
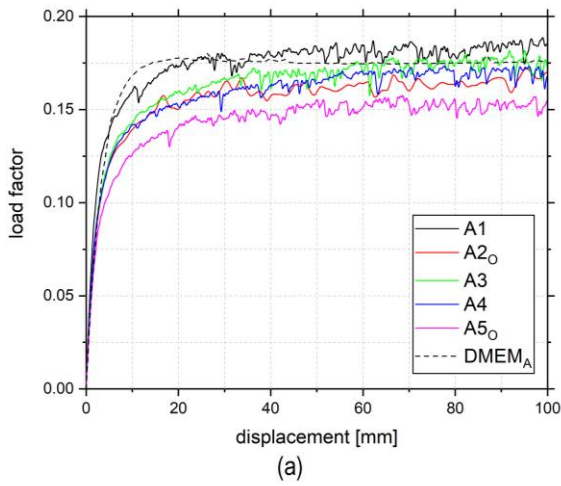
394

## 395 4.2 Nonlinear static analysis

396 Nonlinear static analyses have been performed applying an incremental lateral force, proportional to  
397 the mass of the structure, in X+ direction (Figure 8). Figure 8 also represents the control point used to  
398 define the pushover curves, which corresponds to the middle node at the top of the longitudinal wall  
399 that exhibits the maximum out of plane displacement.

400 Figure 11a and Figure 11b report the pushover curves for classes A and B characterised by a different  
401 number on the units' courses equal to 18 and 12, respectively. As stated above, for each class, five  
402 masonry patterns characterised by an increased index of randomness and the presence of openings have  
403 been generated (Figure 10). Results demonstrate how irregular masonry patterns, as well as the presence  
404 of the openings, tend to decrease the capacity of the structures.

405 As mentioned earlier, reference macro-element mesh discretisation has been compared with the random  
406 generated models (A2, A3, B2, B3) as well as with regular mesoscale configuration (A1, B1). To this  
407 end, reverse engineering was considered for selected mechanical parameters to get a good match in  
408 terms of structural response between macroscale and mesoscale models. In order to simulate the  
409 interlocking effect, in the macroscale model, the shear-diagonal behaviour has been calibrated  
410 according to a Turnsek-Cacovic failure criterion assuming a perfectly post-elastic law. The shear  
411 strength in the absence of axial load has been assumed to be equal 0.2 MPa while a value of 0.6 has  
412 been considered for the friction coefficient  $\mu_s$ . The tensile strength  $f_t$  and the cohesion  $c$ , which affected  
413 the peak of the capacity curve, have been increased to 0.025 MPa in macro-model A and to 0.015 MPa  
414 in macro-model B with the aim to satisfactorily reproduce the static nonlinear response of the mesoscale  
415 models A1 and B1, respectively. Moreover, the value of tensile fracture energy  $G_{ft}$ , which influenced  
416 the post-peak capacity as reported in Ref. [49], was increased to 0.25 and 0.30 N/mm in the constitutive  
417 law of model A and B, respectively. It is worth noting that the interlocking phenomenon effect on the  
418 initial stiffness is less pronounced than the previously analysed U-shape. It happens because the  
419 interlocking phenomenon tends to increase the structure's initial stiffness, particularly when the  
420 slenderness ratio is small.



421

422 Figure 11: Comparison in terms of load-displacement curves for classes A and B characterised by a different  
 423 number on the units' courses equal to: (a) 18; (b) 12.

424

425

426

427

428

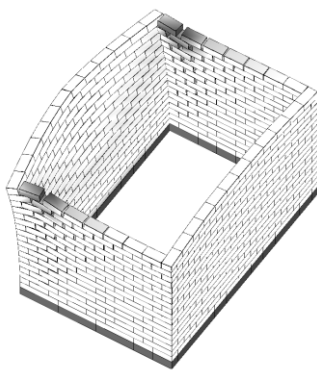
429

430

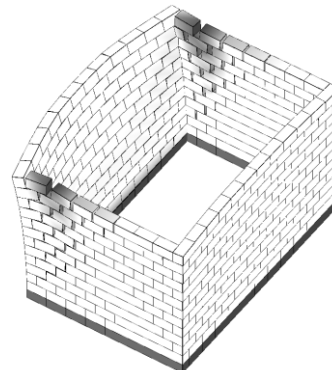
431

432

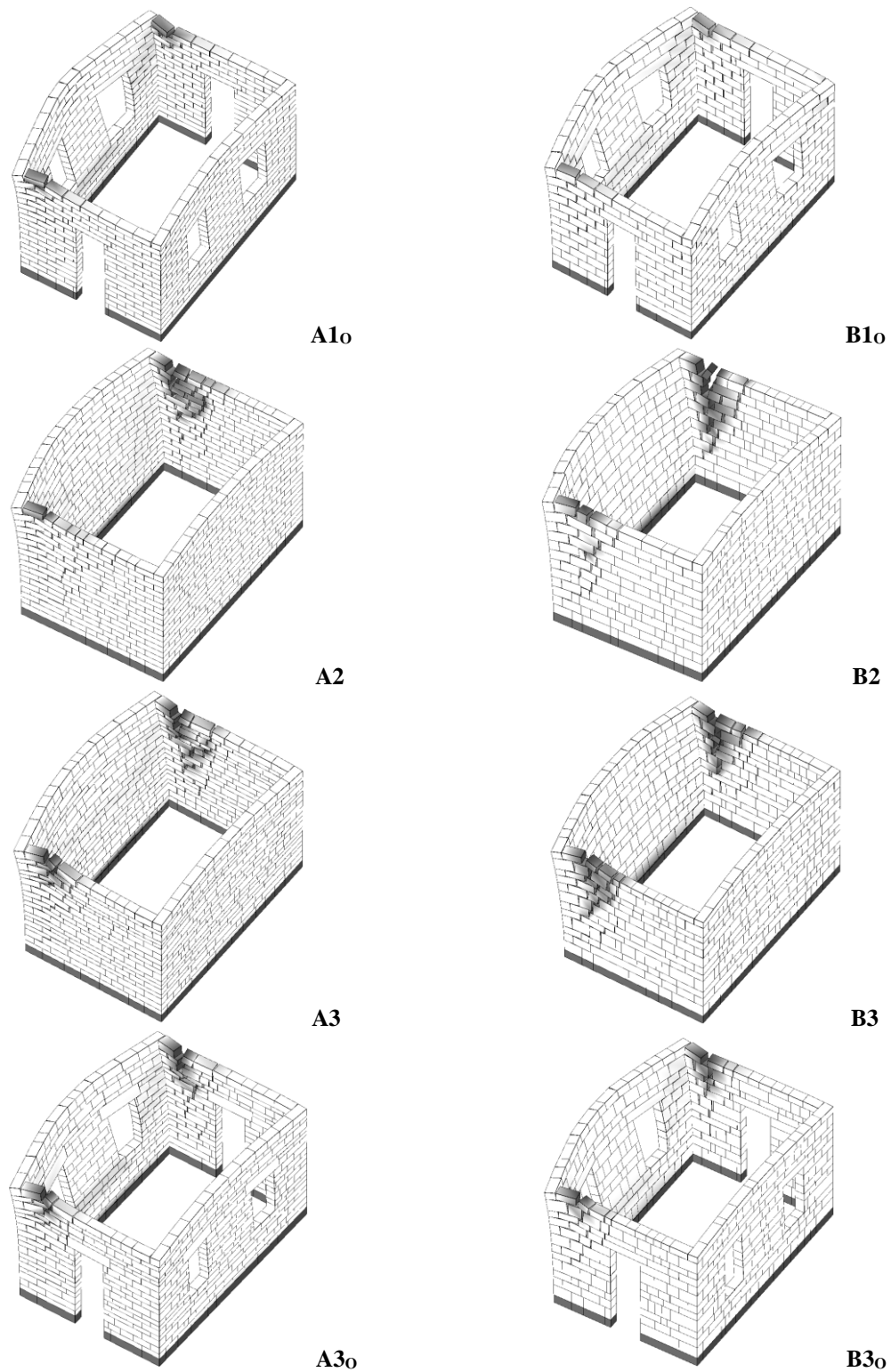
Furthermore, the deformed shapes at the last step of the analyses, highlighting the collapse mechanisms of the structures and the concentration of plastic strains, are reported in Figure 12. The failure mechanisms are always characterised by the overturning of the wall orthogonally loaded and subjected to outwards actions. In this regard, it is observed how the plastic strains are mainly concentrated at the connection with the sidewalls. It is worth noting how increasing the randomness index, the collapse mechanism is more localised at a single wall, and the structure tends to rapidly lose the box behaviour, whereas, in the structure with a regular masonry pattern, the overall structural behaviour is affected by a more global character although the incipient collapse mechanism is still characterised by the collapse of the wall that tends to overturn OOP.



**A1**

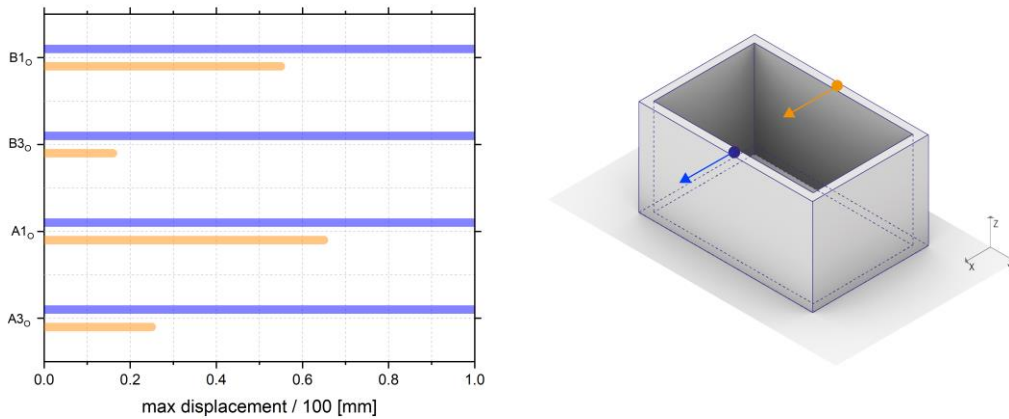


**B1**



433  
 434 Figure 12: Deformed shapes of the mesh discretisations adopted for control point displacement equal to 100 mm.  
 435 For the sake of clarity, the histogram reported in Figure 13 represents the maximum displacement  
 436 reached at the end of the simulations for the mesh configuration A1<sub>o</sub> and A3<sub>o</sub> evaluated by monitoring  
 437 two control points located in the middle of the two opposite long walls. The same analysis has been

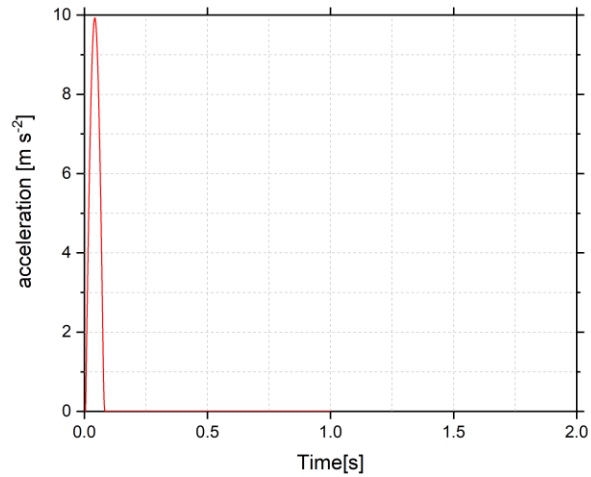
438 reported regarding the configuration B1<sub>o</sub> and B3<sub>o</sub>. In both cases, the results have been normalised with  
 439 respect to the greater of the maximum displacements reached by the two points, and they quantitatively  
 440 demonstrate how a chaotic distribution tends to localise the collapse mechanism leading to a negative  
 441 influence on the masonry prototypes' global behaviour.



442  
 443 Figure 13: Comparisons in terms of maximum displacement reached: orange vs blue control point. Notation 1  
 444 indicates a regular masonry pattern and notation 3 indicates an irregular masonry pattern.

### 445 4.3 Nonlinear dynamic analysis

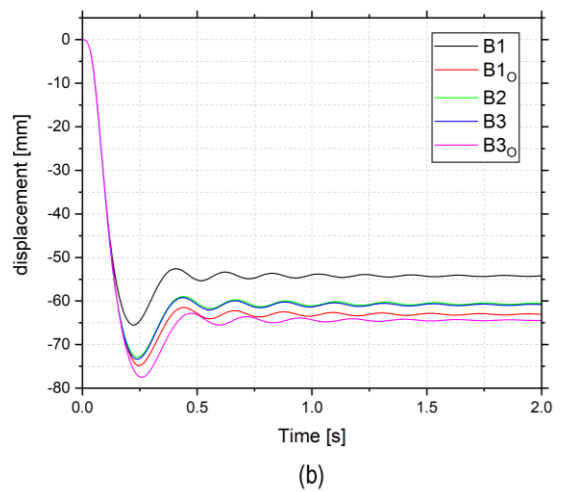
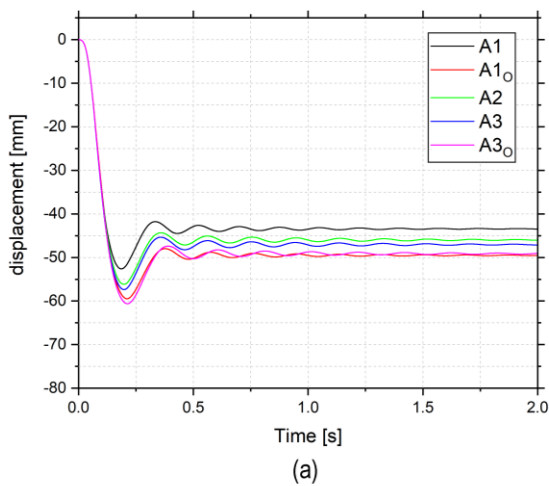
446 In this section, dynamic simulations have been performed applying a semi-sinusoidal pulse with an  
 447 amplitude equal to 1g and a frequency of 6.7 Hz (that is a frequency close to the first mode vibration of  
 448 the model A1) as input ground motion along the X direction (see Figure 14). Newmark's method with  
 449 parameters  $\gamma = 0.5$  and  $\beta = 0.25$  [61], and a time step of 0.005 s has been adopted as numerical  
 450 integration procedure, whereas the energy dissipation was based on the Rayleigh viscous damping  
 451 criterion [62], assuming a 5% damping ratio associated with the 1<sup>st</sup> and 13<sup>th</sup> natural frequencies, the  
 452 latter corresponding to 80% of the total accumulated specimen mass.



453

454 Figure 14: Ground motion input: semi-sinusoidal pulse.

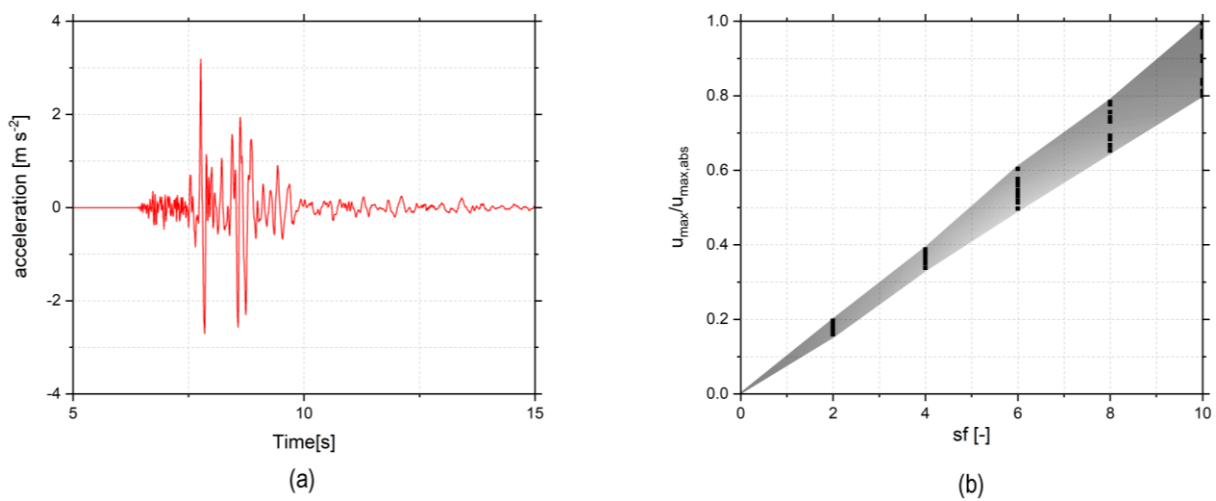
455 Figure 15 a and b report the time-history displacement of the control point of the mesoscale patterns  
 456 belonging to classes A and B. Similar to what is underlined within the nonlinear static analyses (with  
 457 lower capacity in terms of forces), the mesh discretisations belonging to class B (low number of units'  
 458 courses) show higher residual displacements. Indeed, B models are affected statistically by a smaller  $m$   
 459 parameter, i.e., the ratio between the half-length and height of the blocks, being class B characterised  
 460 by fewer courses. It results in an overall lower capability of the blocks to generate frictional resistance  
 461 in their plane [63].



462

463 Figure 15: Comparison in terms of time history displacement.

464 Figure 15a and Figure 15b show how increasing the masonry pattern's randomness, the structures are  
 465 affected by larger displacements. Similarly, larger displacements are found in cases with openings, for  
 466 which the structures are obviously affected by lower global stiffness. Finally, aiming to investigate the  
 467 dynamic response of the considered specimens when subjected to earthquake loading, incremental  
 468 dynamic analysis (IDA) has been carried out by adopting the Amatrice EW (2016) earthquake record,  
 469 Italy, as input ground motion active along the X-direction (see Figure 16a). The original record has been  
 470 scaled in order to reach the condition of the near-collapse of the investigated masonry prototype.



471  
 472 Figure 16: (a) Amatrice EW (2016) record; (b) ratio between the maximum displacement of the control point and  
 473 the absolute maximum displacement for all mesh discretisations as a function of the scale factor of the record:  
 474 shaded red provides the envelope of the results.

475 Figure 16b reports the ratio between the maximum displacement of the control point and the absolute  
 476 maximum displacement for all the investigated adopted mesh discretisations as a function of the scale  
 477 factor of the record, which is a measure of the ground motion intensity (IM). It should be underlined  
 478 that the adopted mesh configurations have shown a divergent behaviour with the increase of the scale  
 479 factor, pointing out that the influence of the mesh pattern is larger, in terms of the maximum reached  
 480 displacement, for a higher value of PGA. The results also confirm the need to perform stochastic  
 481 simulations by generating a large number of masonry pattern configurations statistically consistent.

## 482 **5 Final remarks**

483 This paper investigates the DMEM approach by adopting a mesoscale representation rather than a  
484 classical macroscale representation. At first, parametric analyses investigate the mesh sensitivity of the  
485 DMEM approach and shed light on the mechanical parameters that need to be calibrated to consider  
486 physical phenomena, namely interlocking behaviour generated by the vertical joint misalignment. Such  
487 investigations were performed by using a benchmark model represented by a U-shape masonry  
488 prototype made in stone, idealising the experimental tests performed at the LNEC shaking table [55].  
489 The results underlined the need to recalibrate the tensile fracture energy as well as the tensile strength.  
490 Furthermore, the comparisons with a classical FE homogeneous model calibrated in ABAQUS showed  
491 that DMEM requires much lower computational demand, also if the adopted discrete modelling  
492 approach contemplated a unit by unit mesoscale modelling.

493 In order to adequately simulate URM structures characterised by units with variable dimensions, a  
494 random masonry pattern generator was developed and implemented in a GHPython script. Such a script  
495 was adopted to generate 10 masonry prototypes (with different level of randomness), with the overall  
496 dimension consistent with a rectangular plan having 4.80 m and 7.20 m and walls' height equal to 4.0  
497 m, in order to evaluate how the chaotic distribution of the units might affect the structural behaviour.  
498 Both nonlinear static and dynamic analyses were performed, and the results demonstrated how the  
499 masonry pattern affected the structural response. In particular, it was worth noting how the increase of  
500 the randomness degree generated an early loss of the box behaviour.

501 The main conclusions of this study are that:

- 502 1. DMEM approach is able to take into account the main in-plane and out-of-plane failure  
503 mechanisms;
- 504 2. Mesoscale configurations have been compared with a classical macro-element mesh  
505 discretisation. To this end, it was necessary to calibrate some mechanical parameters in order  
506 to get a good match in terms of structural response.
- 507 3. A digital tool was adopted to generate random masonry patterns; it can generate chaotic  
508 masonry patterns by defining a few parameters.

- 509 4. The results demonstrated how the arrangement of the blocks affected the results. Moreover, by  
510 increasing the randomness index, the collapse mechanism is localised, and the structures lose  
511 the box behaviour, whereas, in the structure with a regular masonry pattern, the overall  
512 structural behaviour exhibited a more global character.
- 513 5. Further investigations are necessary to better understand the potential of the DMEM approach  
514 in handling a mesoscale model and to have a clear picture of the influence of mesh discretisation  
515 on mechanical properties.
- 516 6. Further efforts are also required to implement a masonry pattern generator by taking into  
517 account geometrical parameters easily detectable from practitioners, i.e., masonry quality index  
518 [64].

519 Future studies could include: i) statistical definition of the mechanical properties [65], [66]; ii)  
520 simulation of strengthening techniques, such as the use of Textile Reinforced Matrix (TRM) or Fiber  
521 Reinforced Polymers (FRP) reinforcement, for masonry pattern having units of variable dimensions.

#### 522 **Author contribution statement:**

523 **Federica Vadalà:** Conceptualisation, Methodology, Software, Writing—Original draft preparation,  
524 Validation. **Valeria Cusmano:** Conceptualisation, Methodology, Software, Visualisation, Writing—  
525 Original draft preparation, Validation, Writing—Original draft preparation. **Marco Francesco Funari:**  
526 Conceptualisation, Methodology, Software, Random mesh generator Visualisation, Supervision,  
527 Validation, Writing—Original draft preparation, Writing—Reviewing and Editing. **Ivo Calìo:**  
528 Software, Writing—Reviewing and Editing. **Paulo B. Lourenço:** Writing—Reviewing and Editing. All  
529 authors have read and agreed to the published version of the manuscript.

#### 530 **Funding:**

531 This work was partly financed by FCT/MCTES through national funds (PIDDAC) under the R&D Unit  
532 Institute for Sustainability and Innovation in Structural Engineering (ISISE), under reference  
533 UIDB/04029/2020.

534 This work was partly funded by project STAND4HERITAGE that has received funding from the  
535 European Research Council (ERC) under the European Union's Horizon 2020 research and innovation  
536 programme (Grant agreement No. 833123), as an Advanced Grant.

537 This research was partially supported by the EWAS Project "an Early WARNING System for Cultural  
538 Heritage" (ARS021\_00926) PNR 2015-2020 Area di Specializzazione" CULTURAL HERITAGE".  
539 CUP E66C18000380005.

540

## 541 **References**

542 [1] M. Milić *et al.*, "Assessment and Rehabilitation of Culturally Protected Prince Rudolf Infantry  
543 Barracks in Zagreb after Major Earthquake," *Build 2021, Vol 11, Page 508*, vol. 11, no. 11, p.  
544 508, Oct. 2021, doi: 10.3390/BUILDINGS11110508.

545 [2] L. Lulić, K. Ožić, T. Kišiček, I. Hafner, and M. Stepinac, "Post-Earthquake Damage  
546 Assessment—Case Study of the Educational Building after the Zagreb Earthquake," *Sustain*  
547 *2021, Vol 13, Page 6353*, vol. 13, no. 11, p. 6353, Jun. 2021, doi: 10.3390/SU13116353.

548 [3] M. Diaferio, D. Foti, M. F. Sabbà, and M. Lerna, "A procedure for the seismic risk assessment  
549 of the cultural heritage," *Bull Earthq Eng*, vol. 19, no. 2, pp. 1027–1050, 2021.

550 [4] S. Silvestri *et al.*, "Shaking table testing of groin vaults made by 3D printers," *Soil Dyn Earthq*  
551 *Eng*, vol. 150, p. 106880, 2021.

552 [5] D. Foti and V. Vacca, "EXPERIMENTAL INVESTIGATION OF THE SEISMIC RESPONSE  
553 OF A MULTI-DRUM COLUMN," *WIT Trans Eng Sci*, vol. 118, pp. 11–19, 2017.

554 [6] S. Sharma, L. C. Silva, F. Graziotti, G. Magenes, and G. Milani, "Modelling the experimental  
555 seismic out-of-plane two-way bending response of unreinforced periodic masonry panels using  
556 a non-linear discrete homogenized strategy," *Eng Struct*, vol. 242, p. 112524, Sep. 2021, doi:  
557 10.1016/J.ENGSTRUCT.2021.112524.

558 [7] J. A. Dauda, L. C. Silva, P. B. Lourenço, and O. Iuorio, "Out-of-plane loaded masonry walls  
559 retrofitted with oriented strand boards: Numerical analysis and influencing parameters," *Eng*  
560 *Struct*, vol. 243, p. 112683, 2021.

561 [8] G. Fortunato, M. F. Funari, and P. Lonetti, "Survey and seismic vulnerability assessment of the

- 562 Baptistery of San Giovanni in Tumba (Italy),” *J Cult Herit*, vol. 26, pp. 64–78, 2017, doi:  
563 10.1016/j.culher.2017.01.010.
- 564 [9] D. Malomo, A. Mehrotra, and M. J. DeJong, “Distinct element modeling of the dynamic  
565 response of a rocking podium tested on a shake table,” *Earthq Eng Struct Dyn*, vol. 50, no. 5,  
566 pp. 1469–1475, 2021.
- 567 [10] A. M. D’altri *et al.*, “Modeling Strategies for the Computational Analysis of Unreinforced  
568 Masonry Structures: Review and Classification,” vol. 27, pp. 1153–1185, 2020, doi:  
569 10.1007/s11831-019-09351-x.
- 570 [11] S. Karimzadeh, K. Kadas, A. Askan, M. A. Erberik, and A. Yakut, “Derivation of analytical  
571 fragility curves using SDOF models of masonry structures in Erzincan (Turkey),” *Earthquakes*  
572 *Struct*, vol. 18, no. 2, pp. 249–261, 2020.
- 573 [12] L. Cascini, R. Gagliardo, and F. Portioli, “LiABlock\_3D: A Software Tool for Collapse  
574 Mechanism Analysis of Historic Masonry Structures,” *Int J Archit Herit*, vol. 14, no. 1, pp. 75–  
575 94, 2020, doi: 10.1080/15583058.2018.1509155.
- 576 [13] G. De Felice and R. Giannini, “Out-of-plane seismic resistance of masonry walls,” *J Earthq*  
577 *Eng*, vol. 5, no. 2, pp. 253–271, 2001, doi: 10.1080/13632460109350394.
- 578 [14] C. Casapulla, L. Cascini, F. Portioli, and R. Landolfo, “3D macro and micro-block models for  
579 limit analysis of out-of-plane loaded masonry walls with non-associative Coulomb friction,”  
580 2014, doi: 10.1007/s11012-014-9943-8.
- 581 [15] M. F. Funari, L. C. Silva, E. Mousavian, and P. B. Lourenço, “Real-time Structural Stability of  
582 Domes through Limit Analysis: Application to St. Peter’s Dome,”  
583 <https://doi.org/10.1080/15583058.2021.1992539>, pp. 1–23, Oct. 2021, doi:  
584 10.1080/15583058.2021.1992539.
- 585 [16] A. Giuffrè, “A Mechanical Model for Statics and Dynamics of Historical Masonry Buildings,”  
586 in *Protection of the Architectural Heritage Against Earthquakes*, Springer Vienna, 1996, pp.  
587 71–152.
- 588 [17] D. D’Ayala and E. Speranza, “Definition of Collapse Mechanisms and Seismic Vulnerability of  
589 Historic Masonry Buildings,” *Earthq Spectra*, vol. 19, no. 3, pp. 479–509, 2003, doi:

- 590 10.1193/1.1599896.
- 591 [18] M. F. Funari, A. Mehrotra, and P. B. Lourenço, “A Tool for the Rapid Seismic Assessment of  
592 Historic Masonry Structures Based on Limit Analysis Optimisation and Rocking Dynamics,”  
593 *Appl Sci*, vol. 11, no. 3, p. 942, Jan. 2021, doi: 10.3390/app11030942.
- 594 [19] M. F. Funari, S. Spadea, P. Lonetti, F. Fabbrocino, and R. Luciano, “Visual programming for  
595 structural assessment of out-of-plane mechanisms in historic masonry structures,” *J Build Eng*,  
596 vol. 31, Sep. 2020, doi: 10.1016/j.jobe.2020.101425.
- 597 [20] M. F. Funari, S. Spadea, M. Ciantia, P. Lonetti, and F. Greco, “Visual programming for the  
598 structural assessment of historic masonry structures,” 2020.
- 599 [21] G. Fortunato, M. F. Funari, and P. Lonetti, “Survey and seismic vulnerability assessment of the  
600 Baptistery of San Giovanni in Tumba (Italy),” *J Cult Herit*, 2017, doi:  
601 10.1016/j.culher.2017.01.010.
- 602 [22] L. C. Silva, N. Mendes, P. B. Lourenço, and J. Ingham, “Seismic Structural Assessment of the  
603 Christchurch Catholic Basilica, New Zealand,” *Structures*, vol. 15, pp. 115–130, Aug. 2018, doi:  
604 10.1016/J.ISTRUC.2018.06.004.
- 605 [23] S. Szabó, A. Kövesdi, Z. Vasáros, Á. Csicsely, and D. Hegyi, “The cause of damage and failure  
606 of the Mud-brick vault of the Khan in New-Gourna,” *Eng Fail Anal*, vol. 128, p. 105567, Oct.  
607 2021, doi: 10.1016/J.ENGFAILANAL.2021.105567.
- 608 [24] M. F. Funari, A. E. Hajjat, M. G. Masciotta, D. V. Oliveira, and P. B. Lourenço, “A Parametric  
609 Scan-to-FEM Framework for the Digital Twin Generation of Historic Masonry Structures,”  
610 *Sustain 2021, Vol 13, Page 11088*, vol. 13, no. 19, p. 11088, Oct. 2021, doi:  
611 10.3390/SU131911088.
- 612 [25] M. Lerna, M. F. Sabbà, M. Diaferio, L. Carnimeo, S. Ivorra, and D. Foti, “Seismic risk  
613 assessment of a medieval tower: The case study of Craco,” 2020.
- 614 [26] N. Hoveidae, A. Fathi, and S. Karimzadeh, “Seismic damage assessment of a historic masonry  
615 building under simulated scenario earthquakes: A case study for Arge-Tabriz,” *Soil Dyn Earthq*  
616 *Eng*, vol. 147, p. 106732, 2021, doi: <https://doi.org/10.1016/j.soildyn.2021.106732>.
- 617 [27] P. Roca, M. Cervera, L. Pelà, R. Clemente, and M. Chiumenti, “Continuum FE models for the

- 618 analysis of Mallorca Cathedral,” *Eng Struct*, vol. 46, pp. 653–670, Jan. 2013, doi:  
619 10.1016/j.engstruct.2012.08.005.
- 620 [28] J. V. Lemos, “Discrete element modeling of masonry structures,” *Int J Archit Herit*, vol. 1, no.  
621 2, pp. 190–213, 2007, doi: 10.1080/15583050601176868.
- 622 [29] J. V. Lemos, “Discrete element modeling of the seismic behavior of masonry construction,”  
623 *Buildings*, vol. 9, no. 2, 2019, doi: 10.3390/buildings9020043.
- 624 [30] T. T. Bui, A. Limam, V. Sarhosis, and M. Hjiij, “Discrete element modelling of the in-plane  
625 and out-of-plane behaviour of dry-joint masonry wall constructions,” *Eng Struct*, vol. 136, no.  
626 October, pp. 277–294, 2017, doi: 10.1016/j.engstruct.2017.01.020.
- 627 [31] S. Gonen, B. Pulatsu, E. Erdogmus, E. Karaesmen, and E. Karaesmen, “Quasi-static nonlinear  
628 seismic assessment of a fourth century A.D. Roman Aqueduct in Istanbul, Turkey,” *Heritage*,  
629 vol. 4, no. 1, pp. 401–421, 2021, doi: 10.3390/heritage4010025.
- 630 [32] J. Kim, F. Lorenzoni, M. Salvalaggio, and M. R. Valluzzi, “Seismic vulnerability assessment of  
631 free-standing massive masonry columns by the 3D Discrete Element Method,” *Eng Struct*, vol.  
632 246, p. 113004, 2021, doi: <https://doi.org/10.1016/j.engstruct.2021.113004>.
- 633 [33] F. Clementi, V. Gazzani, M. Poiani, and S. Lenci, “Assessment of seismic behaviour of heritage  
634 masonry buildings using numerical modelling,” *J Build Eng*, vol. 8, pp. 29–47, Dec. 2016, doi:  
635 10.1016/j.jobe.2016.09.005.
- 636 [34] S. Chen, A. Ferrante, F. Clementi, and K. Bagi, “DEM analysis of the effect of bond pattern on  
637 the load bearing capacity of barrel vaults under vertical loads,” *Int J Mason Res Innov*, vol. 6,  
638 no. 3, pp. 346–373, 2021.
- 639 [35] D. Foti, V. Vacca, and I. Facchini, “DEM modeling and experimental analysis of the static  
640 behavior of a dry-joints masonry cross vaults,” *Constr Build Mater*, vol. 170, pp. 111–120, 2018.
- 641 [36] N. Savalle, É. Vincens, and S. Hans, “Experimental and numerical studies on scaled-down dry-  
642 joint retaining walls: Pseudo-static approach to quantify the resistance of a dry-joint brick  
643 retaining wall,” *Bull Earthq Eng*, vol. 18, no. 2, pp. 581–606, 2020.
- 644 [37] V. Sarhosis, J. V Lemos, and K. Bagi, “Chapter 13 - Discrete element modeling,” in *Woodhead*  
645 *Publishing Series in Civil and Structural Engineering*, B. Ghiassi and G. B. T.-N. M. of M. and

- 646 H. S. Milani, Eds. Woodhead Publishing, 2019, pp. 469–501.
- 647 [38] P. B. Lourenço and L. C. Silva, “Computational applications in masonry structures: From the  
648 meso-scale to the super-large/super-complex,” *Int J Multiscale Comput Eng*, vol. 18, no. 1, pp.  
649 1–30, 2020, doi: 10.1615/IntJMultCompEng.2020030889.
- 650 [39] M. F. Funari, L. C. Silva, N. Savalle, and P. B. Lourenço, “A concurrent micro/macro FE-model  
651 optimized with a limit analysis tool for the assessment of dry-joint masonry structures,” *Int J*  
652 *Multiscale Comput Eng*, vol. In Press, 2022, doi: 10.1615/IntJMultCompEng.2021040212.
- 653 [40] D. Malomo and M. J. DeJong, “A Macro-Distinct Element Model (M-DEM) for simulating the  
654 in-plane cyclic behavior of URM structures,” *Eng Struct*, vol. 227, no. April 2020, p. 111428,  
655 2021, doi: 10.1016/j.engstruct.2020.111428.
- 656 [41] A. M. D’Altri, N. Lo Presti, N. Grillanda, G. Castellazzi, S. de Miranda, and G. Milani, “A two-  
657 step automated procedure based on adaptive limit and pushover analyses for the seismic  
658 assessment of masonry structures,” *Comput Struct*, vol. 252, p. 106561, Aug. 2021, doi:  
659 10.1016/j.compstruc.2021.106561.
- 660 [42] D. Malomo and M. J. DeJong, “A Macro-Distinct Element Model (M-DEM) for out-of-plane  
661 analysis of unreinforced masonry structures,” *Eng Struct*, vol. 244, no. April, p. 112754, 2021,  
662 doi: 10.1016/j.engstruct.2021.112754.
- 663 [43] E. Quagliarini, G. Maracchini, and F. Clementi, “Uses and limits of the Equivalent Frame Model  
664 on existing unreinforced masonry buildings for assessing their seismic risk: A review,” *J Build*  
665 *Eng*, vol. 10, pp. 166–182, Mar. 2017, doi: 10.1016/J.JOBE.2017.03.004.
- 666 [44] R. Siano *et al.*, “Numerical investigation of non-linear equivalent-frame models for regular  
667 masonry walls,” *Eng Struct*, vol. 173, pp. 512–529, 2018, doi:  
668 <https://doi.org/10.1016/j.engstruct.2018.07.006>.
- 669 [45] I. Calì, M. Marletta, and B. Pantò, “A new discrete element model for the evaluation of the  
670 seismic behaviour of unreinforced masonry buildings,” *Eng Struct*, vol. 40, pp. 327–338, 2012,  
671 doi: 10.1016/j.engstruct.2012.02.039.
- 672 [46] B. Pantò, F. Cannizzaro, I. Calì, and P. B. Lourenço, “Numerical and Experimental Validation  
673 of a 3D Macro-Model for the In-Plane and Out-Of-Plane Behavior of Unreinforced Masonry

674 Walls,” *Int J Archit Herit*, vol. 11, no. 7, pp. 946–964, 2017, doi:  
675 10.1080/15583058.2017.1325539.

676 [47] F. Cannizzaro, B. Pantò, S. Caddemi, and I. Calì, “A Discrete Macro-Element Method  
677 (DMEM) for the nonlinear structural assessment of masonry arches,” *Eng Struct*, vol. 168, no.  
678 October 2020, pp. 243–256, 2018, doi: 10.1016/j.engstruct.2018.04.006.

679 [48] C. Chàcara, P. B. Lourenço, B. Pantò, F. Cannizzaro, and I. Calì, “Macro-element mass matrix  
680 for the dynamic assessment of unreinforced masonry structures,” 2017.

681 [49] B. Pantò, L. Silva, G. Vasconcelos, and P. B. Lourenço, “Macro-modelling approach for  
682 assessment of out-of-plane behavior of brick masonry infill walls,” *Eng Struct*, vol. 181, no.  
683 November 2018, pp. 529–549, 2019, doi: 10.1016/j.engstruct.2018.12.019.

684 [50] C. Chàcara, F. Cannizzaro, B. Pantò, I. Calì, and P. B. Lourenço, “Seismic vulnerability of  
685 URM structures based on a Discrete Macro-Element Modeling (DMEM) approach,” *Eng Struct*,  
686 vol. 201, p. 109715, Dec. 2019, doi: 10.1016/j.engstruct.2019.109715.

687 [51] F. Cannizzaro, “The seismic behavior of historical buildings: a macro-element approach,”  
688 University of Catania, 2010.

689 [52] V. Turnšek and F. Čačovič, “Some experimental results on the strength of brick masonry walls,”  
690 *Proc 2nd Int Brick Mason Conf*, pp. 149–156, 1971.

691 [53] I. Calì and B. Pantò, “A macro-element modelling approach of Infilled Frame Structures,”  
692 *Comput Struct*, vol. 143, pp. 91–107, 2014, doi: 10.1016/j.compstruc.2014.07.008.

693 [54] F. Peña, “A Semi-Discrete Approach for the Numerical Simulation of Freestanding Blocks,” no.  
694 June, pp. 416–439, 2016, doi: 10.4018/978-1-5225-0231-9.ch016.

695 [55] P. X. Candeias, A. Campos Costa, N. Mendes, A. A. Costa, and P. B. Lourenço, “Experimental  
696 assessment of the out-of-plane performance of masonry buildings through shaking table tests,”  
697 *Int J Archit Herit*, vol. 11, no. 1, pp. 31–58, 2017.

698 [56] F. Cannizzaro and P. B. Lourenço, “Simulation of Shake Table Tests on Out-of-Plane Masonry  
699 Buildings. Part (VI): Discrete Element Approach,”  
700 <https://doi.org/10.1080/15583058.2016.1238973>, vol. 11, no. 1, pp. 125–142, Jan. 2016, doi:  
701 10.1080/15583058.2016.1238973.

- 702 [57] V. Abaqus, “6.14 Documentation,” *Dassault Syst Simulia Corp*, vol. 651, no. 6.2, 2014.
- 703 [58] S. Cattari *et al.*, “Nonlinear modeling of the seismic response of masonry structures: critical  
704 review and open issues towards engineering practice,” *Bull Earthq Eng*, 2021.
- 705 [59] G. Milani and P. B. Lourenço, “A simplified homogenized limit analysis model for randomly  
706 assembled blocks out-of-plane loaded,” *Comput Struct*, vol. 88, no. 11, pp. 690–717, 2010, doi:  
707 <https://doi.org/10.1016/j.compstruc.2010.02.009>.
- 708 [60] “The Python Language Reference — Python 3.9.5 documentation,” 2021.  
709 <https://docs.python.org/3/reference/> (accessed Jun. 15, 2021).
- 710 [61] N. M. Newmark, “A Method of Computation for Structural Dynamics,” *J Eng Mech Div*, vol.  
711 85, no. 3, pp. 67–94, Jul. 1959, doi: 10.1061/JMCEA3.0000098.
- 712 [62] A. Alipour and F. Zareian, “Study rayleigh damping in structures; uncertainties and treatments,”  
713 in *the 14th world conference on earthquake engineering*, 2008, pp. 12–17.
- 714 [63] C. Casapulla and L. U. Argiento, “In-plane frictional resistances in dry block masonry walls and  
715 rocking-sliding failure modes revisited and experimentally validated,” *Compos Part B Eng*, vol.  
716 132, pp. 197–213, Jan. 2018, doi: 10.1016/J.COMPOSITESB.2017.09.013.
- 717 [64] A. Borri and A. De Maria, “L’indice di Qualità Muraria (IQM): Evoluzione ed Applicazione  
718 nell’Ambito delle Norme Tecniche per le Costruzioni del 2008,” 2009.
- 719 [65] B. Pulatsu, S. Gonen, E. Erdogmus, P. B. Lourenço, J. V. Lemos, and R. Prakash, “In-plane  
720 structural performance of dry-joint stone masonry Walls: A spatial and non-spatial stochastic  
721 discontinuum analysis,” *Eng Struct*, vol. 242, p. 112620, Sep. 2021, doi:  
722 10.1016/J.ENGSTRUCT.2021.112620.
- 723 [66] B. Pulatsu, S. Gonen, E. Erdogmus, P. B. Lourenço, J. V. Lemos, and J. Hazzard, “Tensile  
724 Fracture Mechanism of Masonry Wallettes Parallel to Bed Joints: A Stochastic Discontinuum  
725 Analysis,” *Model 2020, Vol 1, Pages 78-93*, vol. 1, no. 2, pp. 78–93, Oct. 2020, doi:  
726 10.3390/MODELLING1020006.
- 727